Engineering sulfur vacancies optimization in $Ni_3Co_6S_8$ nanospheres toward extraordinarily efficient nitrate electroreduction to ammonia

Weixiang Tao, Peifang Wang [*], Hao Li, Rong Huang, Gang Zhou [*]

Key Laboratory of Integrated Regulation and Resource Development on Shallow Lake of Ministry of Education, College of Environment, Hohai University, Nanjing 210098, People's Republic of China

ARTICLE INFO

ABSTRACT

Electrocatalytic nitrate reduction into recyclable ammonia (NH_3) plays a critical role in maintaining the global nitrogen balance and meeting the growing energy demand. However, the research on controllable defects of traditional semiconductor electrocatalytic materials remains lacking, resulting in limiting nitrate reduction reaction (NO_3RR) activity. Herein, we develop a facile electrical joule heating method to flexibly regulate the sulfur vacancies (SVs) content on the surface of $Ni_3Co_6S_8$ (NCS), in which SVs can regulate the electronic structure of NCS. Therefore, more $3d$ electrons can be localized at Co sites that can reduce the energy barrier of the rate-determining step ($HNO_3* \rightarrow NO_2*$). As a result, the NCS with reasonable SVs concentration exhibits the outstanding selectivity (98.2%), Faradaic efficiency (85.3%) and yield rate (2388.4 µg h^{-1} cm^{-2}) for electrocatalytic nitrate reduction to ammonia while maintaining their structural integrity. This work provides a new insight for addressing both nitrate pollution and ammonia energy production.

1. Introduction

Ammonia (NH_3), as one of the largest chemicals produced in the world, can not only be utilized as amino fertilizer to achieve high yield of crops, but also as energy storage medium [1,2]. This is of great significance to the development of ammonia energy production [3,4]. Presently, ammonia is mainly produced on a large scale through the Haber-Bosch process in industry [5]. This traditional production technology needs to break the nitrogen-nitrogen triple bond ($N \equiv N$) (the dissociation energy = 941 kJ mol^{-1}) under harsh conditions (high temperature (350–550 ℃) and pressure (150–350 atm)) [6,7], resulting in high energy consumption and limiting the efficient synthesis of ammonia [8,9]. Nitrate (NO_3^-), which exists widely industrial and domestic wastewater [10,11], is an attractive alternative with lower $N=O$ bond dissociation energy of 204 kJ mol^{-1} [12]. Thus, using nitrate as nitrogen source to produce ammonia by electrocatalytic reduction under environmental conditions is an ingenious approach [13,14]. The reasonable design and development electrocatalysts with high activity and selectivity for electrocatalytic reduction of nitrate to ammonia are significant [15–17].

To date, various metal oxides [18,19], metal phosphides [20,21] and bimetallic compounds [22,23] display great potential for electrocatalysis of nitrate to ammonia. However, the present electrocatalysts for NO_3RR still suffer from poor reactivity and low ammonia yield [24–26]. In recent years, the construction of engineering intrinsic defects is becoming an effective strategy to enhance the catalytic activity of electrocatalytic reduction of nitrate to ammonia synthesis [27–29]. As a kind of special intrinsic defects, anion vacancy can weaken the coulomb force between adjacent cations and anions, thus regulating the electronic structure and improving the activity of the catalyst [30,31]. Recently, Jia et al. suggest that the oxygen vacancy in titanium dioxide nanotubes with rich oxygen vacancies (TiO_{2-x}) are filled with oxygen atoms in nitrate to weaken the $N=O$ bonds and achieving high selectivity of ammonia synthesis through nitrate reduction [32]. The defects of oxygen vacancies in RuO_2 nanosheets with disordered structure are recently proposed by Wang et al. [33] to adjust the D-band center and hydrogen affinity, thus speeding up the potential-determining step of conversion ($NH_2 * \rightarrow NH_3 *$). However, there are few studies to improve the NO_3RR activity of bimetallic catalysts by modulating SVs.

Herein, $Ni_3Co_6S_8$ nanospheres with sulfur-rich vacancies (NCS-2) growing on a nickel foam (NF) substrate are successfully fabricated. The Faradaic efficiency (85.3%) and ammonia yield rate (2388.4 ug h^{-1} cm^{-2}) of NCS-2 are 2.2 and 5.1 times that of the pristine NCS, respectively. ^{15}N isotope labeling experiments indicate that ammonia originate

---

in nitrate. Ammonia is quantitatively analyzed by the ^{1}H nuclear magnetic resonance (NMR) spectra and continuous-flow analysis (CFA). The intermediates are detected by online differential electrochemical mass spectrometry (DEMS) to infer reaction pathways. X-ray photoelectron spectroscopy (XPS) and integrated-crystal orbital Hamilton population (ICOHP) results indicate that Co is more likely to accumulate more reactive charges in the active sites, promoting the formation of NO_2^* and increasing the energy barrier required for hydrogen formation. In addition, the density functional theory (DFT) calculations reveal that the adsorption energy of NCS- 2 for NO_2^* is enhanced by formation of SVs. Therefore, the NCS-2 shows superior activity and selectivity in electrocatalytic reduction of nitrate to ammonia.

2. Experimental section

2.1. Synthesis of Ni3Co6S8 (NCS) grown on nickel foam (NF)

The NCS needle-like nanospheres grown on NF were synthesized by modifying the method reported previously [34,35]. A commercial NF (1 × 2 cm^2) was treated by 3 M HCl for 12 h, and repeatedly rinsed with deionized water (H$_2$O) and dried at 60 °C for 8 h. 4.8 mmol Ni (NO$_3$)$_2$·6H$_2$O, 9.6 mmol Co(NO$_3$)$_2$·6H$_2$O, 20 mmol urea and 16 mmol NH$_4$F were dissolved in 40 mL H$_2$O under stirring to form a light red solution. The NF was immersed in the above solution for ultrasonic 15 min, then stirred for 2 h. Then it was transferred to a 50 mL Teflon-lined stainless-steel autoclave at 100 ℃ for 12 h in an electric oven. After electric oven cooled down to room temperature, the NF with catalytic washed with deionized water and ethanol for several times to remove surface impurities, which dried overnight at 60 ℃. In order to obtain Ni$_3$Co$_6$S$_8$, the assynthesized NiCo-precursor was then sulfurized. 12.8 mmol Na$_2$S·9 H$_2$O were dissolved in 40 mL of deionized water under stirring. Then the solution was transferred to a 50 mL Teflon-lined stainless-steel autoclave, where NF with NiCo-precursor was vertically arranged at 140 ℃ for 6 h. After electric stove chilled off to room temperature, the NF with Ni$_3$Co$_6$S$_8$ catalytic washed with deionized water and ethanol for a few times, which vacuum dried overnight at 60 ℃.

2.2. Synthesis of Ni3Co6S8-x (NCS-x) grown on NF

The NF (1 × 2 cm^2) loaded NCS was placed on Joule heating device (JH 3.1), and the NCS was vacuum heated at 500 ℃, 700 ℃ and 1000 ℃ under DC voltage of 30 V and DC current of 80 A. The samples were named NCS-1, NCS-2 and NCS-3 according to different heating temperatures. Similarly, NF-x were named NF-1, NF-2 and NF-3, respectively.

2.3. Electrochemical nitrate reduction measurements

Nafion 115 membrane (DuPont) was used to assemble the H-type cell. Electrochemical measurements were performed using an electrochemical workstation (CIMPS, Zahner, Germany) at room temperature and atmospheric pressure. The as-prepared materials were used as a working electrode. Platinum foil (2 × 2 cm^2) and Ag/AgCl/KCl (saturated KCl electrolyte) were used as the counter electrode and the reference electrode. The electrolytes were Ar-saturated 1 M KOH (pH = 13.65) containing different concentrations of NO$_3$-N. The electrode area was 1 × 2 cm^2 for tests in 20–1000 mg L^{-1} nitrate. Dilute sulfuric acid and potassium hydroxide solution were used to adjust the pH of electrolytic. All potentials measured against Ag/AgCl were converted to the reversible hydrogen electrode (RHE) scale using E(RHE) = E(Ag/AgCl) + E^0(Ag/AgCl) + 0.059 pH [36], where E^0(Ag/AgCl) was the standard electrode potential of Ag/AgCl reference electrode. Solution resistance was determined by potentiostatic electrochemical impedance spectroscopy and manually compensated for polarization curves. Before nitrate electroreduction test, linear sweep voltammetry (LSV) curves were

performed until that the polarization curves achieved steady-state ones at a rate of 5 mV s^{-1} from 0.5 to − 0.5 V vs. RHE. Potentiostatic measurements were performed for 2 h in 60 mL cathode electrolyte with a stirring rate of 300 rpm, and then the electrolyte was stored at 4 °C (no more than 2 days) before analysis. The product concentrations, including nitrite, nitrite, and ammonium, after reaction were analyzed.

2.4. Density functional theory (DFT) calculations

The Vienna Ab-inito Simulation Package (VASP) was used for all the DFT calculations. The Perdew-Burke-Ernzerhof (PBE) function in the generalized gradient approximation (GGA) method was used to describe the exchange-correlation effects. The projected augmented wave (PAW) method was used to calculate the core-valence interaction. The energy cutoff for plane wave expansions was set to 500 eV, and kpoints of the 3 × 3 × 3 Monkhorst-Pack grids were selected to sample the Brillouin zone integration. The vacuum space surfaces more than 15 Å were used to avoid periodic interactions. The structural optimization of energy and force convergence sets were completed at 1.0×10^{-4} eV and 0.02 eV Å^{-1}, respectively.

The following formula was used to calculate the Gibbs free energy change (ΔG) of each step:

$$\Delta G = \Delta E + \Delta ZPE - T\Delta S \quad (1)$$

Where ΔE represents the electronic energy difference directly calculated by the DFT, ΔZPE is the zero point energy difference, T is the room temperature (298.15 K) and ΔS is the entropy change. ZPE could be obtained after frequency calculation by:

$$ZPE = \frac{1}{2}\sum hvi \quad (2)$$

And the TS values of adsorbed species were calculated via the vibration frequency:

$$
\begin{aligned}
TS &= K_B T \left[C + D + 1 \right] \\
C &= \sum_k \ln\left(\frac{1}{1 - e^{\frac{hv}{k_B T}}} \right) \\
D &= \sum_k \frac{hv}{k_B T} \frac{1}{\left(e^{\frac{hv}{k_B T}} - 1 \right)}
\end{aligned}
\quad (3)
$$

3. Results and discussion

3.1. Synthesis and characterization of NCS-x

The formation process of the Ni$_3$Co$_6$S$_8$ nanospheres with sulfur-rich vacancies is schematically displayed in Fig. 1a. Firstly, NiCo-based precursors on nickel foam (NF) substrate are prepared by a facile hydrothermal method. Subsequently, coulomb attraction urges negatively charged S atoms to selectively bond with NiCo species, finally leading to the formation of bimetallic sulfide Ni$_3$Co$_6$S$_8$. Afterward, NCS-x (x = 1, 2 and 3 depending on the heating temperature) with SVs are constructed by accelerating the escape of S atoms on NCS surface with joule heating device. The Xray diffraction (XRD) pattern of NCS in Fig. 1b displays that the diffraction peaks of NCS at 15.4°, 29.7°, 31.0°, 39.3°, 47.4° and 51.8° are indexed to the (111), (311), (222), (331), (511) and (440) facets of Ni$_3$Co$_6$S$_8$ phase (JCPDS No. 12–0723), respectively. It's worth noting that the phase structures of NCS-1 and NCS-2 remain unchanged significantly with the increase of heating temperature. However, when the temperature reaches 1000 ℃, the characteristic peaks of CoS$_{1.035}$ (JCPDS No. 25–1081) are observed in the XRD spectrum of NCS-3 (Fig. S4). The scanning electron microscopy (SEM) in Fig. 1c and the transmission electron microscopy (TEM) in Fig. 1d of NCS-2 reveal that NF is covered by needle-like nanospheres with a diameter about 3 μm. In addition, it can be observed from Fig. S5 that the surface of the samples
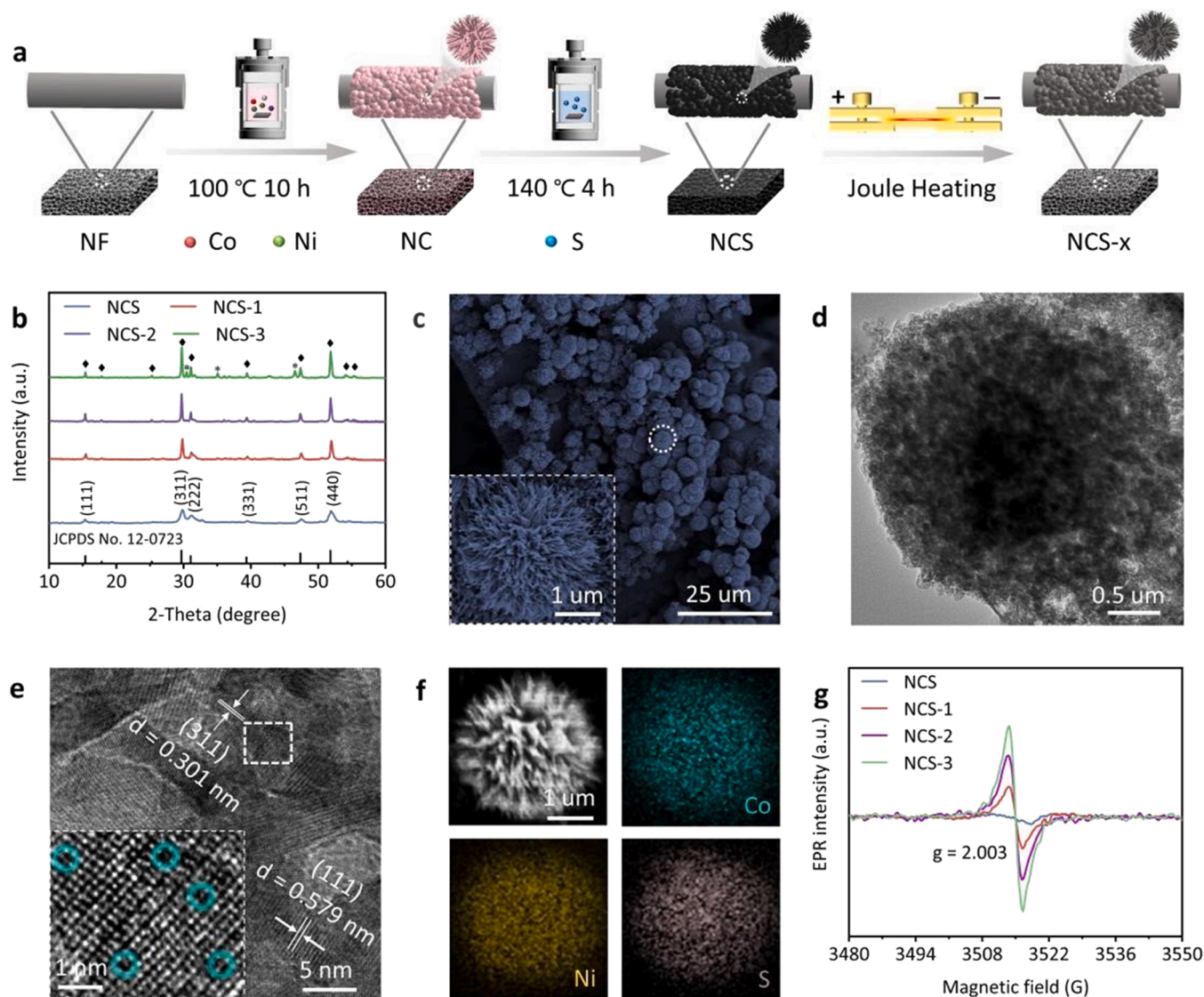
Fig. 1. a) Schematic diagram of NCS-x preparation process. b) XRD pattern for NCS and NCS-x. c) SEM, d) TEM, e) HRTEM images of NCS-2 and f) corresponding EDS elemental mapping images. Inset: SEM enlarged image of the white circle area and HRTEM enlarged image of the white rectangular region. g) EPR spectra of NCS and NCS-x.

obtained below 700 °C retain the needle-like nanospheres morphology. In the high-resolution TEM (HRTEM) images of NCS-2 (Fig. 1e), the lattice spacing of 0.579 nm and 0.301 nm is attributed to the (111) and (311) planes of $Ni_3Co_6S_8$, respectively. Besides, the HRTEM inset in Fig. 1e confirms that the defect lattices (denoted by light bule targeting circles) are irregularly scattered on the NCS-2. The energy dispersive X-ray spectroscopy (EDS) and inductively coupled plasma optical emission spectroscopy (ICP-OES) are used to further characterize the elemental composition and content of the prepared materials. As the element mapping (Fig. 1f) images show that Co, Ni and S are uniformly distributed in NCS-2 nanospheres. According to EDS and ICP-OES analysis (Fig. S6a and Table S1), the element ration of Ni: Co: S in NCS is close to 3: 6: 8. More importantly, the sulfur atom content of the pristine NCS is 48.9%. With the rises of treatment temperature, the sulfur atom contents of NCS-1, NCS-2 and NCS-3 are decreased by 47.23%, 45.72% and 43.94%, respectively (Fig. S6). However, the Co/Ni atomic ration remains stable at ~ 1.6 (Table S2). This indicates that S atoms in NCS are gradually stripped away with the formation of SVs, which is further verified via electron paramagnetic resonance (EPR) spectroscopy (Fig. 1g). The EPR signal at g = 2.003 belongs to the SVs, which can be attributed to the increase of the concentration of unpaired electrons in

the NCS surface as the joule heat treatment temperature rises [37]. Therefore, the signal enhancement means that the SVs content increases, which is consistent with EDS and ICP-OES results.

The defect states of NCS-x and the electronic states of Co and Ni are further identified using X-ray photoelectron spectroscopy (XPS). The presence of Ni, Co and S are confirmed by the XPS survey spectra in a series of $Ni_3Co_6S_8$ samples (Fig. S7). The S 2p spectrum of the pristine NCS can be divided into four characteristic peaks in Fig. 2a. The peak at 161.62 eV belongs to S $2p_{3/2}$, which is usually associated with typical metal-sulfur (M-S) bonds [38]. The peak at 162.69 eV is attributed to S $2p_{1/2}$, which is generally related to SVs with low coordination at the surface [39]. The peak at 163.78 eV is due to the inevitable oxidation during cobalt-nickel sulfide preparation. It should be noted by fitting S 2p for all samples, the percentages of S $2p_{3/2}$ and S $2p_{1/2}$ varied from 55.2% and 26.3% of NCS to 34.2% and 49.2% of NCS-3, respectively. This indicates that the concentration of SVs can be controlled by modulating temperature. The XPS spectra of Co 2p and Ni 2p display six peaks by the multiplet splitting effect [40]. Two spin-orbit doublets for Co^{2+} (781.24/796.97 eV) and Co^{3+} (778.75/793.66 eV) and two satellites of identified as "Sat." (786.03/802.76 eV) in the Co 2p spectrum can be observed (Fig. 2b). As shown in Fig. 2c, the characteristic peaks of
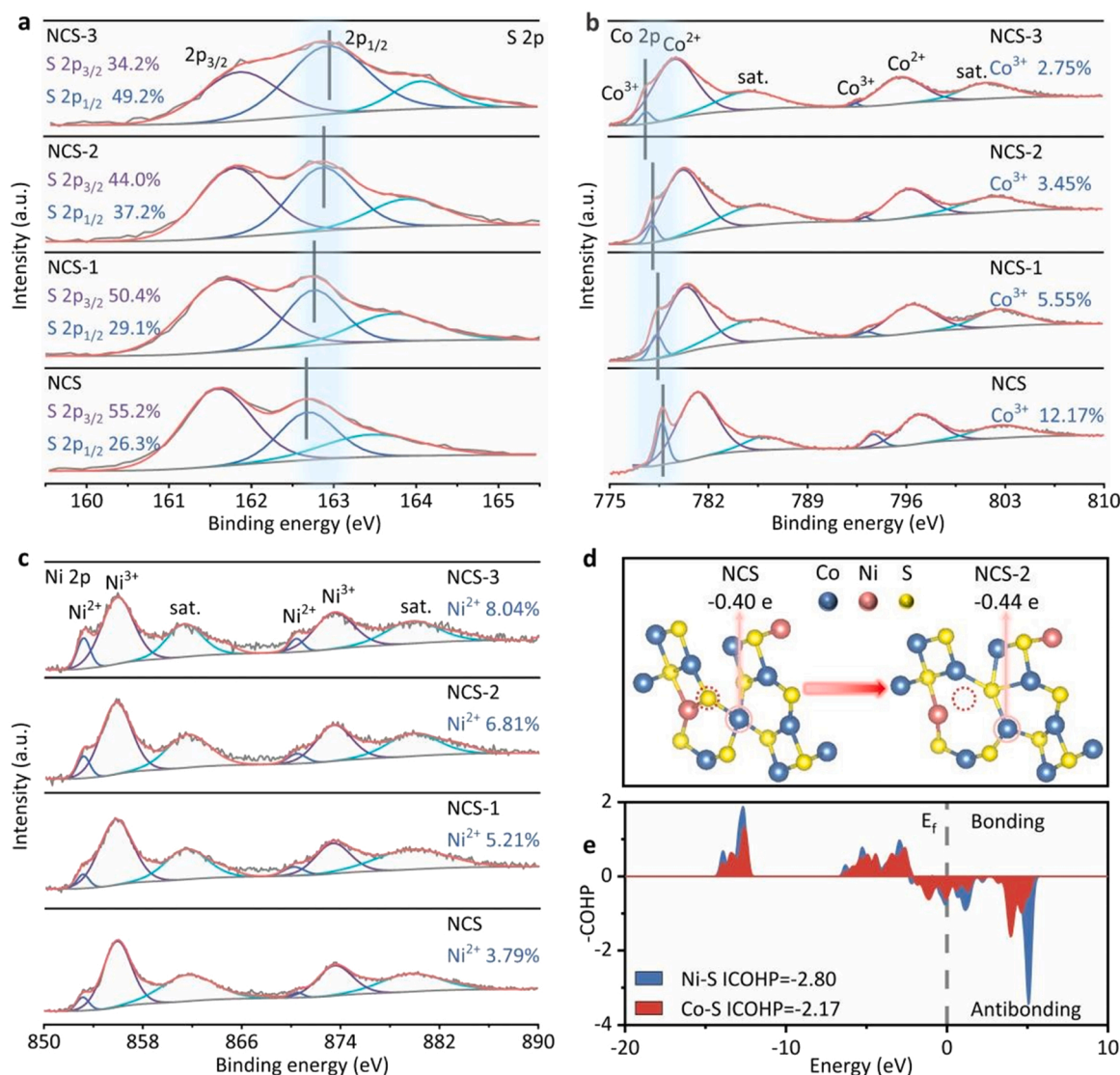
Fig. 2. The XPS spectra of a) S 2p spectra, b) Co 2p spectra and c) Ni 2p spectra of NCS, NCS-1, NCS-2 and NCS-3. d) Bader charges of Co site in NCS and NCS-2. e) The crystal orbital Hamilton population (COHP) of Co-S bond and Ni-S bond in NCS.

Ni^{3+} at 855.99/873.59 eV and Ni^{2+} at 853.12/870.47 eV in the Ni 2p spectra are also deconvoluted. The changes of chemical valence of Ni and Co can also reflect the variation of SVs concentration. From NCS to NCS-3, the percentages of Co^{3+} decreases gradually, while the percentages of Ni^{2+} increases continuously. More importantly, on the NCS-x samples, the binding energy of Ni 2p remains constant while that of Co 2p moves toward lower binding energy and that of S 2p shifts significantly toward higher binding energy, implying that Co accumulate more electrons than Ni and is more likely to be the active site of NO_3RR [41]. As shown in Fig. 2d, the Bader charge analysis discloses that the charge of Co in NCS-2 is − 0.44 e, which is obviously larger than the Co (−0.40 e) in NCS. In addition, by calculating integrated-crystal orbital Hamilton population (ICOHP), the information about the electron energy distribution on the orbital electron density of bonding and antibonding molecular for Co-S and Ni-S bonds in NCS is extracted reliably and efficiently. As shown in Fig. 2e, the ICOHP value of Co-S bonds (−2.17 eV) up to the Fermi level is weaker than that of Ni-S bonds (−2.80 eV), suggesting Co-S bond interaction on the NCS is faintish and more prone to fracture [42]. This further reveals the reason for the impurity signal of $CoS_{1.035}$ in the XRD pattern of NCS-3. Based on the above analysis, it's reasonable to assume that the hybridization between SVs occupied by O atoms of nitrate and Co atoms of NCS-x is more

beneficial than that between the O atoms of nitrate and Ni atoms of NCS-x, and the Co sites with high charge density can accelerate NO_3RR.

3.2. Electrochemical characterization of NCS-x

The electrochemical performance of pristine NCS and NCS-x samples are subsequently evaluated in an alkaline medium (1 M KOH) to determine the influence of SVs on NO_3RR performance. The linear sweep voltammetry (LSV) curves of all samples in 1 M KOH electrolyte containing nitrate display that the initial potential is much lower than that of the hydrogen evolution reaction (HER) without nitrate, and the current density also increases significantly. The NCS-2 exhibits the strongest current density and the lowest initial potential ($\sim$ +0.3 V vs. RHE) during nitrate reduction (Fig. 3a). It is calculated that the Tafel slope decreases to 181 mV dec^{-1} of NCS-2 from 268 mV dec^{-1} of NCS when S atoms are stripped. The Tafel slope of NCS-2 is the smallest among all samples, indicating that its robust nitrate electroreduction kinetics (Fig. 3b). To further confirm this conclusion, the kinetics of as-prepared samples towards NO_3RR are deduced (Fig. S8). The apparent rate constants (k) of NCS-2 are 0.0945 min^{-1}, which is 11.52-folds that of NCS (0.0082 min^{-1}). The double-layer capacitance (C_{dl}) of NCS2 is further evaluated by measuring cyclic voltammetry (CV) curves at
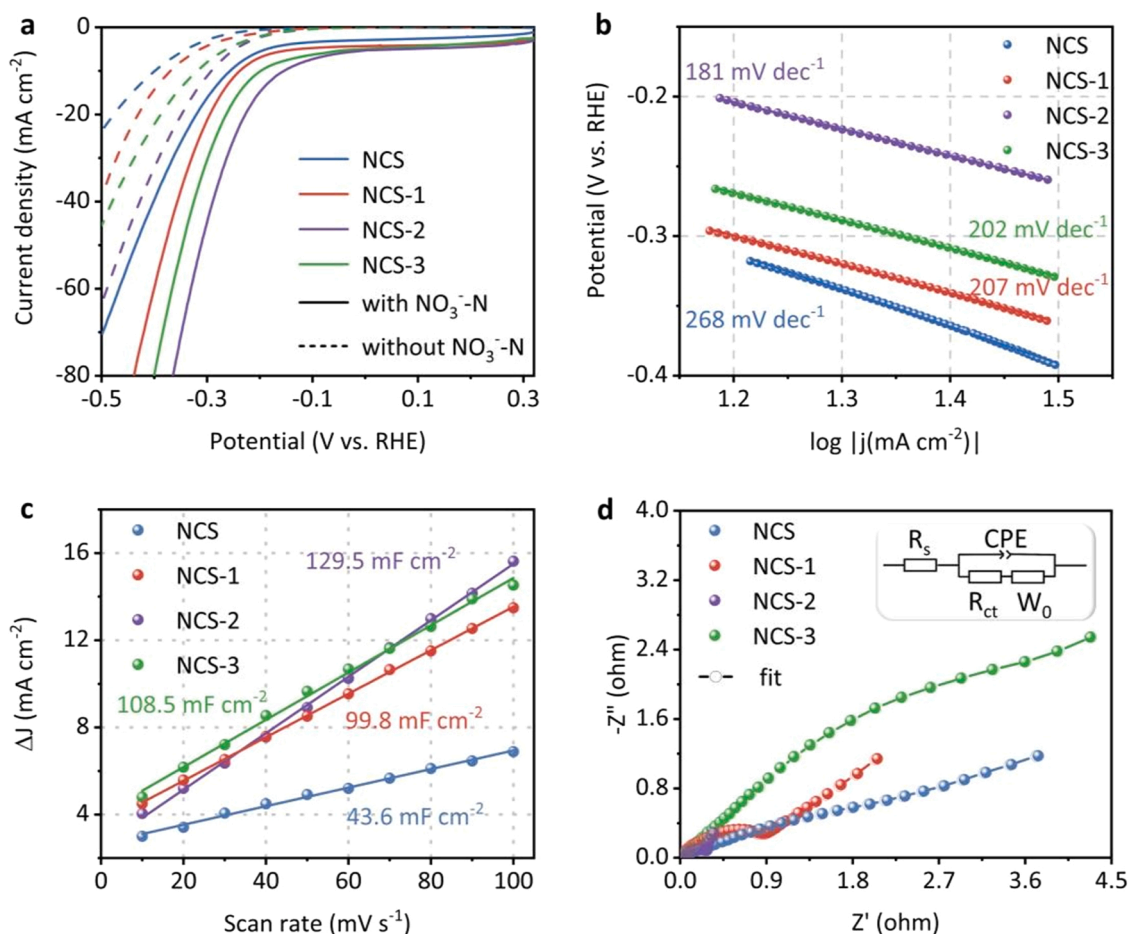
Fig. 3. a) LSV curves of NCS, NCS-1, NCS-2 and NCS-3 in 1 M KOH with and without NO_3^--N. b) Tafel plots, c) linear fitting of capacitive currents, d) EIS Nyquist plots with an equivalent circuit model (inset) for NCS, NCS-1, NCS-2 and NCS-3.

different scan rates ranging from 10 to 100 mV s^{-1} in the potential range without Faradaic current to explore the cause of NCS-2 enhancing NO_3RR (Fig. S9). As shown in Fig. 3c, the C_{dl} value of NCS-2 is 129.5 mF cm^{-2}, much higher than that of NCS (43.6 mF cm^{-2}), NCS1 (99.8 mF cm^{-2}) and NCS-3 (108.5 mF cm^{-2}). According to the calculation method of ECSA, the ECSA values of NCS-1, NCS-2 and NCS-3 are 2.28, 2.97 and 2.48-folds than that of the pristine NCS, recommending the enhanced reactant dynamic locales for NO_3RR. For the Brunauer–Emmett–Teller (BET) surface areas and Barrett–Joyner– Halenda (BJH) pore size distributions of the prepared (Fig. S10), the surface area of the needle-like NCS-2 nanospheres is slightly reduced due to high temperature, but the NCS-2 still maintains mesoporous structure (Table S3). The superior activity might be due to the introduced defect sites on NCS. SVs can shift the previously balanced electrons, thus providing NCS with good electrical conductivity. The surficial resistance of the electrode is defined by the electrochemical impedance spectroscopy (EIS) curves (Fig. 3d). The fitting value of charge-transfer resistance (Rct) for NCS-2 in the high-frequency zone is much smaller than that of other samples (Table S4), indicating that reasonable SVs can accelerate the electron transfer rate at the interface between NCS-2 and nitrate electrolyte. Based on the analysis about electrochemical properties, we can infer that the NCS-2 electrode shows a faster reaction kinetics, lager electrochemical active area and better conductivity, suggesting that NCS-2 can display a more excellent performance in NO_3RR.

3.3. Electrocatalytic performance of ammonia synthesis from nitrate

According to the electrochemical performance results of the pristine NCS and NCS-x, the NCS-2 with appropriate SVs exhibits better electrocatalytic nitrate reduction activity. To determine the optimal potential of NO_3RR, the concentration changes of nitrate, nitrite and ammonia are detected using NCS-2 as cathode electrode at various potentials. The nitrate is more rapidly converted to ammonia and nitrite with the increasing of negatively applied potentials (Fig. S11). Moreover, when the potential changes from − 0.2 V to − 0.5 V vs. RHE, the yield rate of ammonia gradually increases, while the yield rate of nitrite ceaselessly decreases (Fig. 4a). The NCS-2 displays the highest total Faradaic efficiency (86.3%) at − 0.4 V vs. RHE, accompanied by the ammonia yield of 2388.4 µg h^{-1} cm^{-2}. The NO_3RR and HER are both hydrogenation processes, oversize applied potential enhances the hydrogen production process and inhibits the nitrate reduction reaction, thus reducing Faradaic efficiency. To verify this idea, we record CV curves with nitrate solution under varying the starting potentials from − 0.3 to − 0.5 V vs. RHE. There are two oxidation peaks on the CV curves can be observed (Fig. 4b), which can be attributed to oxidation of H_2 and adsorbed H* (H*$_{ads}$), respectively [16,43]. Negligible hydrogen peaks are detected at starting potentials less than − 0.4 V vs. RHE due to inhibition of HER by NO_3RR in alkaline medium. However, as the starting potential rises from − 0.4 V to − 0.5 V vs. RHE, H*$_{ads}$ peaks are significantly diminished but the hydrogen peaks increase correspondingly. The generated H*$_{ads}$ can be widely applied to HER, leading to a cliff drop in the total Faradaic efficiency of NO_3RR. Thus, − 0.4 V vs. RHE is chosen as the optimum operating potential for subsequent studies. The performance of NF substrate, pristine NCS and NCS-x for nitrate reaction action and products formation are investigated as a comparison. First, the contribution of NF substrate to the electrocatalytic reduction of nitrate to ammonia
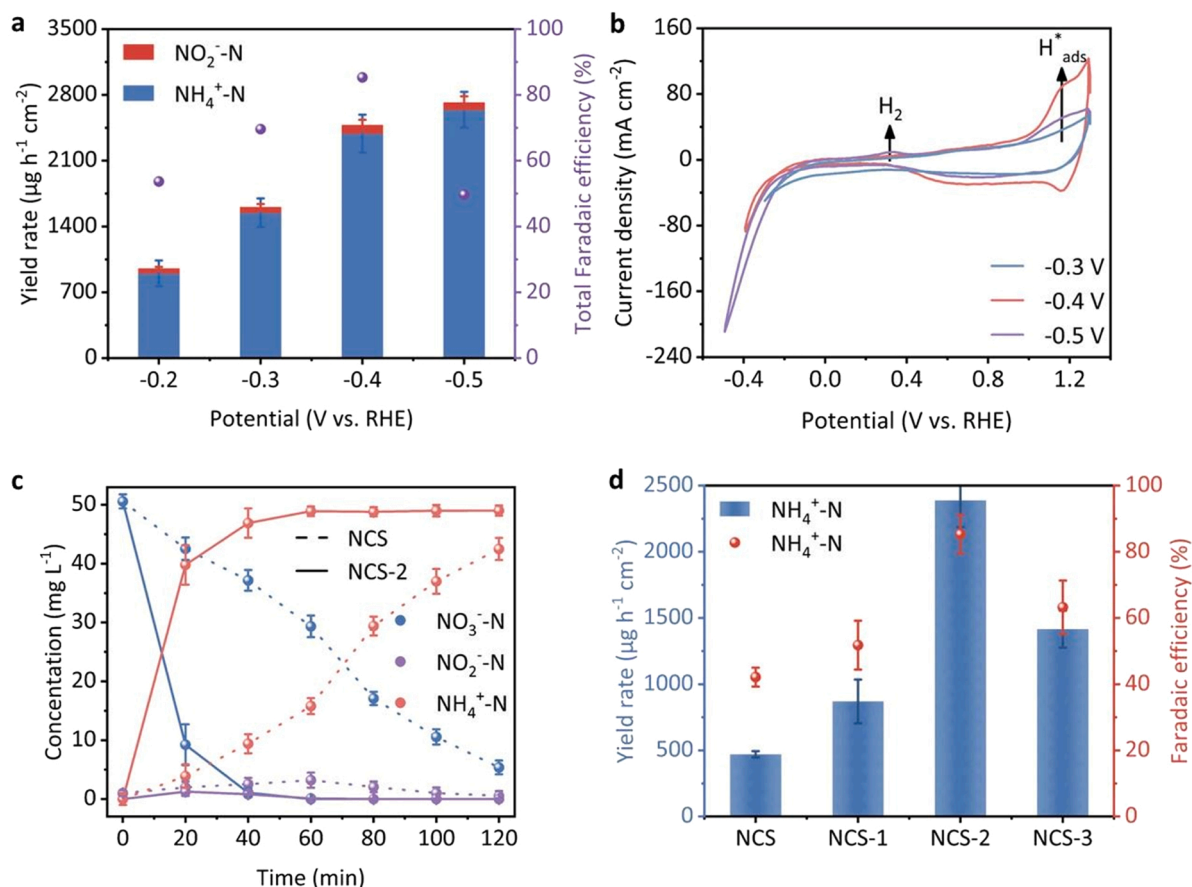
Fig. 4. a) Yield rate and Total Faradaic efficiency, b) CV curves of NCS-2 in 1 M KOH electrolyte with nitrate at different potentials. The starting potential varied from − 0.3 to − 0.5 V vs. RHE. c) Time-dependent concentration of NO_3-N, NO_2-N and NH_4^+-N by NCS and NCS-2 at − 0.4 V vs. RHE. d) Yield rate and Faradaic efficiency of ammonia of NCS, NCS-1, NCS-2 and NCS-3.

can be excluded (Fig. S12). After the formation of SVs, the NCS-2 shows the faster nitrate degradation rate and the highest ammonia yield (Fig. 4c and Fig. S13). Within 60 min, 50 mg L^{-1} NO_3-N is almost completely reduced, accompanied by the production of 46.3 mg L^{-1} NH_4^+-N and 0.8 mg L^{-1} NO_2-N. More importantly, the concentration of nitrite increases and then decreases with the prolongation of reaction time, implying the existence of nitrite as an intermediate product, which is consistent with the results of previous studies [44]. It can be found that the time of the highest nitrite concentration is 20 min in NCS-2, while that is 60 min in NCS. The advance in time is attributed to an increase in the kinetic rate because reduction of nitrate to nitrite by electrocatalytic is the rate-limiting step of NO_3RR [45]. The improvement of NCS-2 performance can be explained by the SVs significantly heightening the electron density of Co sites, breaking the rate-limiting step and accelerating nitrate conversion. To evaluate the influence of the catalyst intrinsic activities on NO_3RR, the yield rate of ammonia is normalized to the actual catalyst loading amount. The normalization results illustrate that NCS-2 still exhibits the maximum yield rate (Fig. S14). In addition, the turnover frequency (TOF) is estimated by normalizing the rate of ammonia formation to the total number of Co ions (Fig. S15). By this method, the TOF of NCS-2 at − 0.4 V vs. RHE is determined to be $8.88 \times 10^{-4}\,s^{-1}$, which is higher 5.16-folds than that of NCS ($1.72 \times 10^{-4}\,s^{-1}$). The experimental results confirm the outstanding intrinsic activity of NCS-2. From Fig. 4d, the NCS-2 with suitable SVs displays the highest Faradaic efficiency (85.3%) and yield rate (2388.4 µg h^{-1} cm^{-2}) of ammonia, compared with NCS (Faradaic efficiency: 42.2%, yield rate: 471.2 µg h^{-1} cm^{-2}), NCS-1 (Faradaic efficiency: 51.8%, yield rate: 870.6 µg h^{-1} cm^{-2}) and NCS-3 (Faradaic efficiency: 63.2%, yield rate: 1416.3 µg h^{-1} cm^{-2}). It is revealing that

excessive SVs destroy the partial structure to form impurities, which results in a certain degradation of catalytic activity.

As shown in Fig. 5a, the influences of NCS-2 on nitrate conversion capacity and ammonia selectivity are investigated at different initial nitrate concentrations. When the concentration of nitrate is less than 200 mg L^{-1}, nitrate conversion and ammonia selectivity of NCS-2 exhibit more than 90%. The NCS-2 demonstrates high nitrate conversion and ammonia selectivity in broad pH (7−14) ranges, yet the nitrate conversion is only ∼ 6.8% at pH 3. The tremendous reduction of nitrate conversion is due to the increase of hydrogen evolution kinetics, which inhibits NO_3RR. The kinetics of HER under acidic electrolytes are 2–3 orders of magnitude higher than that under alkaline electrolyte, hence HER becomes the dominant reaction to prevent nitrate from obtaining electrons for transformation under acidic conditions (Fig. 5b) [46]. The fall slightly in ammonia selectivity may result from nitrogen formation (Fig. S16). According to the results of isotope labeling experiments in Fig. S17, the production of ammonia is unambiguously verified to be from nitrate. The ammonia concentration detected by ^{1}H NMR is very close to the result of CFA method (Fig. S18), which verifies the accuracy of the detection method. The stability of electrocatalyst is one of the important parameters in practical application. The results display that NCS-2 still exhibits high nitrate conversion rate (∼ 100%), ammonia selectivity (∼ 93.35%) and NH_4^+-N Faradaic efficiency (∼ 83.6%) after the six cyclic stability tests under the optimum conditions (Fig. 5c), implying the stability redox activity of NCS-2. In addition, the dissolved Co and Ni concentration in the solution after continuous electrolysis of NCS-2 for 12 h are 10.3 and 40.9 µg L^{-1} (Fig. S19). The leaching concentration of Co and Ni ions are significantly lower than the maximum permissible concentration (1.0 mg L^{-1}) regulated by the
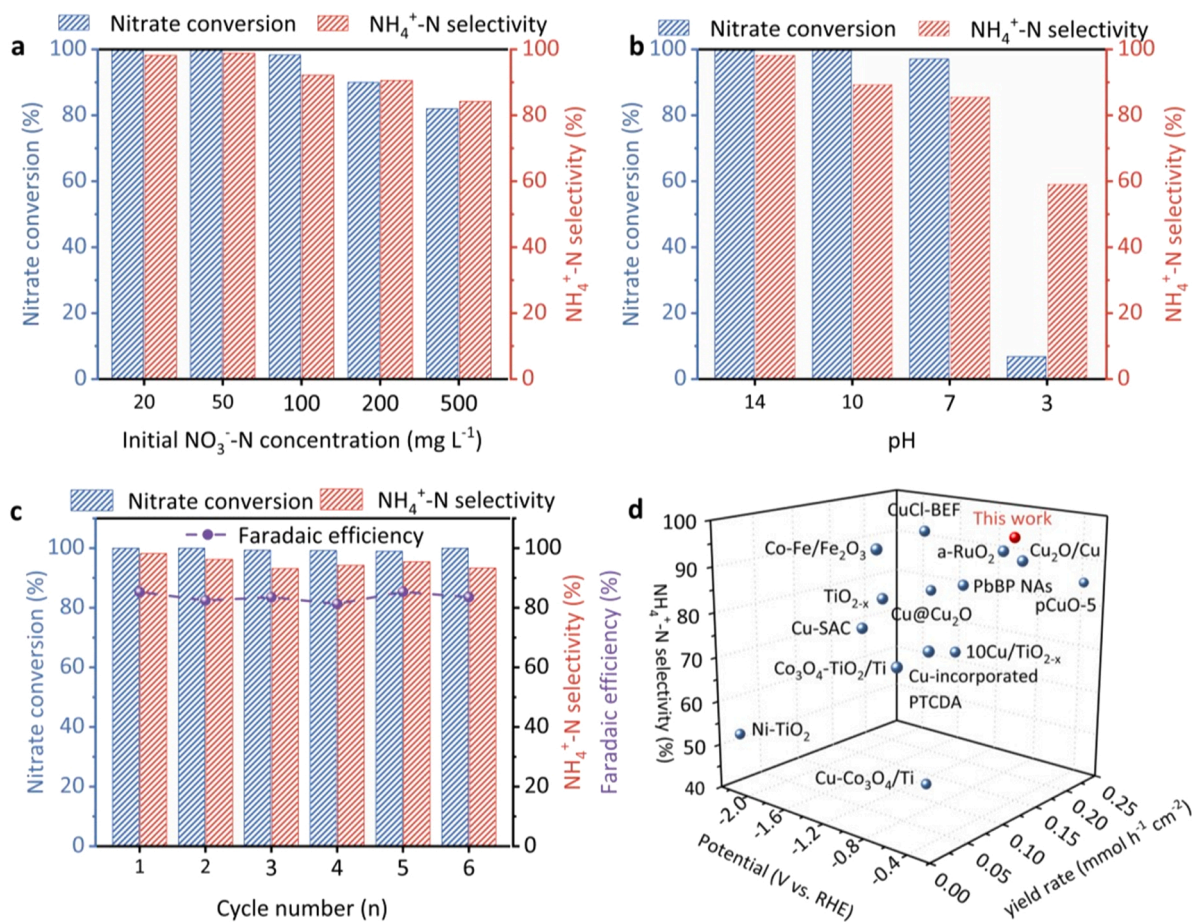
Fig. 5. Effects of a) different initial nitrate concentration and b) different initial pH on nitrate conversion and ammonia selectivity for NO₃RR over NCS-2. c) Consecutive recycling test for NCS-2. Reaction conditions: initial 1 M KOH with 50 mg L^{-1} NO₃-N for (b), (c); cathodic potential = −0.4 V vs. RHE; electrolysis time = 2 h. d) Comparison of applied potential, ammonia selectivity and yield rate of NCS-2 with other reported catalysts.
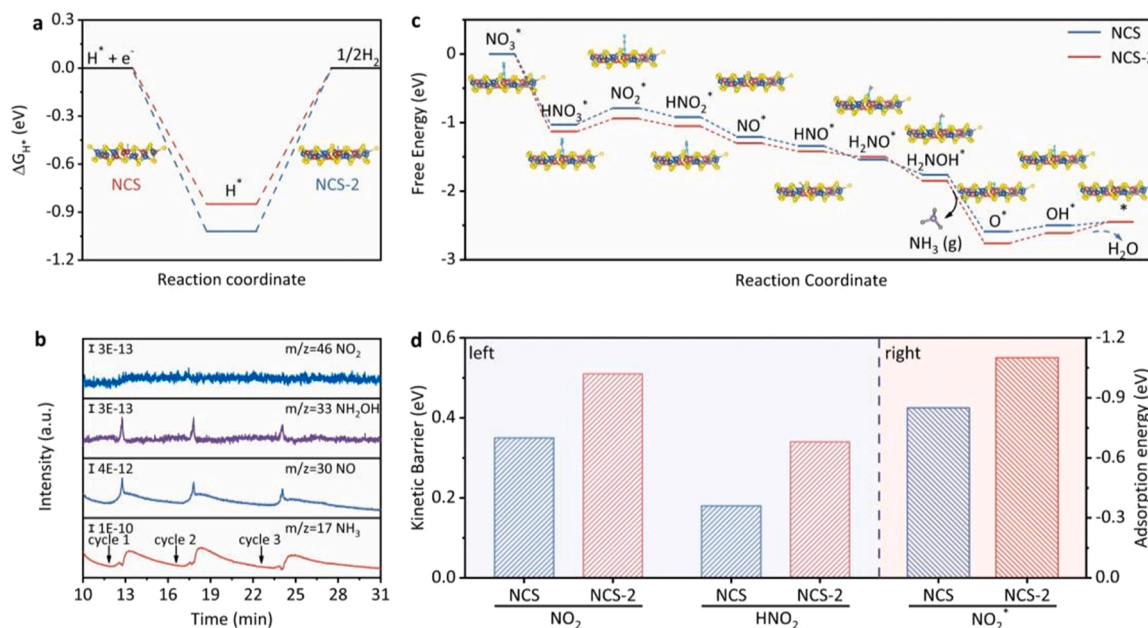

Fig. 6. a) The energies of hydrogen formation on NCS and NCS-2. b) The gaseous intermediate products of NCS-2 in the nitrate reduction reaction are collected and analyzed by DEMS. c) Diagrams of free energy changes for the reaction paths from nitrate reduction to ammonia on NCS and NCS-2. Red, blue, yellow, purple, cyan and gray represents Co, Ni, S, N, O and H, respectively. d) Kinetic barriers of HNO₃* reduction toward NO₂ (g) and HNO₂ (g) formation on the NCS (311) and NCS-2 (311) surfaced (left), and calculated adsorption energies of NO₂* on NCS (311) and NCS-2 (311) surfaces (right).

Emission Standard of Pollutants for Copper, Nickel, Cobalt Industry (GB25467–2010) in China. After several stability tests of NO$_3$RR, the original morphological structure, chemical composition and SVs concentration are unaffected (Fig. S20-22). In addition, NCS-2 with the lower operating potential (−0.4 V vs. RHE), higher ammonia selectivity (98.2%) and ammonia yield rate in electrocatalytic reduction nitrate to ammonia exceeds other reported materials (Fig. 5 d and Table S5).

3.4. Reaction mechanism

In order to probe the origin for the high selectivity and Faradaic efficiency of NCS-2 in the electrocatalytic reduction of nitrate to ammonia, the free energy of the HER on NCS (311) surface and NCS-2 (311) surface are calculated. It is concluded that the free energy for hydrogen adsorption (ΔG_{H*}) on NCS-2 (311) surface is − 1.02 eV, much higher than that of NCS (311) surface (−0.85 eV), indicating that SVs inhibit hydrogen production (Fig. 6a). Thus, the NCS-2 exhibits the high selectivity and Faradaic efficiency in the experiment of ammonia synthesis by NO$_3$RR. Then, in situ electrochemical online differential electrochemical mass spectrometry (DEMS) is used to detect intermediates and products of the reaction. As shown in Fig. 6b, when the baseline kept steady, the mass-to-charge (m/z) ratio signals corresponding to NO, NH$_2$OH and NH$_3$ are 30, 33 and 17, respectively, for three consecutive cycles by applying voltage from 0.2 V to -0.5 V vs. RHE. Besides, the signal belonging to NO$_2$ ($m/z = 46$) is insignificant. Some by-products are also captured (Fig. S24). Based on the DEMS results, the possible nitrate reduction pathways of NCS and NCS-2 are proposed (Fig. 6c). Firstly, NO$_3^-$ is chemically adsorbed on the surface of NCS (311) and NCS-2 (311) surface to form HNO$_3$*. When NO$_3^-$ molecules are transferred to the Co sites, the Co-O bonds are formed [47]. At the same time, the fully occupied Co *3d* orbital in the presence of SVs donates electrons to NO$_3^-$, leading to a significant weakening of the N-O bonds. The coordination bond between O and the neighboring unsaturated Co can be attacked by proton-coupled electron to overcome the energy barrier of the rate-determining step (RDS = 0.19 eV; HNO$_3$*→NO$_2$*) to form NO$_2$*. Notably, NCS-2 can facilitate the formation of NO$_2$* intermediate compared with NCS (RDS = 0.24 eV), thus the reaction facilitates over NCS-2. On the NCS-2 (311) surface, the kinetic energy barrier of the HNO$_3$* to NO$_2$ (0.51 eV) and HNO$_2$ (0.34 eV) is higher than the kinetic energy barrier formation of NO$_2$* (0.19 eV). Because the O atom of HNO$_3$* is bound by the Co site to inhibit the formation of by-products, which is consistent with the fact that NO$_2$ and HNO$_2$ signal is undetected in DEMS. In addition, as shown in Fig. 6d, the low reactivity of NCS compared with NCS-2 may be attributed to the fact that the by-products of NO$_2$ or HNO$_2$ are generated with lower kinetic barriers. For NO$_2$*, the deoxygenation by H* ($k_1 = 7.1 \times 10^8$ M^{-1} s^{-1}) is more than 507-folds larger than that of NO$_3$* ($k_2 = 1.4 \times 10^6$ M^{-1} s^{-1}) [48]. Therefore, the adsorption energy of NO$_2$* on NCS (311) and NCS-2 (311) surfaces are calculated. As shown in Fig. 6d, the adsorption energy of NO$_2$* on NCS-2 (311) is − 1.10 eV, which is much higher than that on NCS (311) (−0.86 eV). This can significantly enhance the adsorption of NO$_2$*. Subsequently, the NO$_2$* rapidly and highly selectively generates the target product NH$_3$ by a series of hydrogenation and deoxidation reactions (NO$_2$*→HNO$_2$*→NO*→HNO*→H$_2$NOH*→ NH$_3$*→NH$_3$) [49]. Finally, the O atoms of Co site combine with H* to generate H$_2$O and then recover SVs (O*→OH*→*) [50]. The conclusion of SVs regeneration is further verified, which is consistent with the results in Fig. S22a.

4. Conclusion

In this work, we report a facile electrical joule heating method to flexibly regulate the SVs contents on the surface of NCS. The NCS-2 with reasonable SVs concentration is reported to exhibit the outstanding selectivity (98.2%), Faradaic efficiency (85.3%) and yield rate (2388.4 µg h^{-1} cm^{-2}) for electrocatalytic reduction of nitrate to ammonia while maintaining their structural integrity. The results of XPS

and ICOHP prove that Co-S bonds are more likely to break than Ni-S bonds, making Co the active site. Combining the analysis of the Bader charge and the adsorption energy of catalysts for NO$_2$*, the SVs can increase the charge density of Co sites and enhance the adsorption of NO$_2$*, reducing the free energy of RDS (HNO$_3$*NO$_2$*) as well as suppressing the HER. Then, the reaction pathway is determined by DFT calculation based on the intermediates captured by online DEMS. This work offers a SVs construction strategy to enhance the catalyst activity, which provides a new insight for addressing both nitrate pollution and ammonia energy production.

CRediT authorship contribution statement

Weixiang Tao: Conceptualization, Methodology, Investigation, Data curation, Formal analysis, Writing – original draft, Validation. **Peifang Wang:** Methodology, Investigation, Data curation, Formal analysis, Writing – original draft, Visualization, Validation. **Hao Li:** Methodology, Investigation, Visualization. **Rong Huang:** Writing – review & editing, Methodology. **Gang Zhou:** Conceptualization, Methodology, Investigation, Data curation, Formal analysis, Funding acquisition, Writing – review & editing, Supervision, Visualization.

Declaration of Competing Interest

The authors declare that they have no known competing financial interests or personal relationships that could have appeared to influence the work reported in this paper.

Data Availability

Data will be made available on request.

Appendix A. Supporting information

Supplementary data associated with this article can be found in the online version at doi:10.1016/j.apcatb.2022.122193.

References

[1] J. Lim, C.A. Fernández, S.W. Lee, M.C. Hatzell, Ammonia and nitric acid demands for fertilizer use in 2050, ACS Energy Lett. 6 (2021) 3676–3685.
[2] J.A. Faria, Renaissance of ammonia synthesis for sustainable production of energy and fertilizers, Curr. Opin. Green. Sust. 29 (2021) 100466.
[3] U.B. Shahid, Y. Bicer, S. Ahzi, A. Abdala, Thermodynamic assessment of an integrated renewable energy multigeneration system including ammonia as hydrogen carrier and phase change material energy storage, Energ. Convers. Manag. 198 (2019) 111809.
[4] F. Chang, W. Gao, J. Guo, P. Chen, Emerging materials and methods toward ammonia-based energy storage and conversion, Adv. Mater. 33 (2021) 2005721.
[5] C. Smith, A.K. Hill, L. Torrente-Murciano, Current and future role of Haber–Bosch ammonia in a carbon-free energy landscape, Energy Environ. Sci. 13 (2020), 331344.
[6] X. Peng, Y. Mi, H. Bao, Y. Liu, D. Qi, Y. Qiu, L. Zhuo, S. Zhao, J. Sun, X. Tang, J. Luo, X. Liu, Ambient electrosynthesis of ammonia with efficient denitration, Nano Energy 78 (2020), 105321.
[7] Y. Li, Q. Zhang, Z. Mei, S. Li, W. Luo, F. Pan, H. Liu, S. Dou, Recent advances and perspective on electrochemical ammonia synthesis under ambient conditions, Small Methods 5 (2021), 2100460.

[8] J.M. Modak, Haber process for ammonia synthesis, Resonance 16 (2011) 1159–1167.

[9] G.F. Chen, Y. Yuan, H. Jiang, S.Y. Ren, L.X. Ding, L. Ma, T. Wu, J. Lu, H. Wang, Electrochemical reduction of nitrate to ammonia via direct eight-electron transfer using a copper–molecular solid catalyst, Nat. Energ. 5 (2020) 605–613.

[10] A.S. Fajardo, P. Westerhoff, C.M. Sanchez-Sanchez, S. Garcia-Segura, Earthabundant elements a sustainable solution for electrocatalytic reduction of nitrate, Appl. Catal. B: Environ. 281 (2021), 119465.

[11] R. Biddau, R. Cidu, S. Da Pelo, A. Carletti, G. Ghiglieri, D. Pittalis, Source and fate of nitrate in contaminated groundwater systems: assessing spatial and temporal variations by hydrogeochemistry and multiple stable isotope tools, Sci. Total Environ. 647 (2019) 1121–1136.

[12] Q. Song, M. Li, X. Hou, J. Li, Z. Dong, S. Zhang, L. Yang, X. Liu, Anchored Fe atoms for NO bond activation to boost electrocatalytic nitrate reduction at low concentrations, Appl. Catal. B: Environ. 317 (2022), 121721.

[13] S. Wei, C. Wan, L. Zhang, X. Liu, W. Tian, J. Su, W. Cheng, Y. Wu, N-doped and oxygen vacancy-rich NiCo2O4 nanograss for supercapacitor electrode, Chem. Eng. J. 429 (2022), 132242.

[14] M. Jiang, Q. Zhu, X. Song, Y. Gu, P. Zhang, C. Li, J. Cui, J. Ma, Z. Tie, Z. Jin, Batch-scale synthesis of nanoparticle-agminated three-dimensional porous Cu@Cu2O microspheres for highly selective electrocatalysis of nitrate to ammonia, Environ. Sci. Technol. 56 (2022) 10299–10307.

[15] J. Cai, Y. Wei, A. Cao, J. Huang, Z. Jiang, S. Lu, S.-Q. Zang, Electrocatalytic nitrate-to-ammonia conversion with ~100% faradaic efficiency via single-atom alloying, Appl. Catal. B: Environ. 316 (2022), 121683.

[16] W. Zheng, L. Zhu, Z. Yan, Z. Lin, Z. Lei, Y. Zhang, H. Xu, Z. Dang, C. Wei, C. Feng, Self-activated ni cathode for electrocatalytic nitrate reduction to ammonia: from fundamentals to scale-up for treatment of industrial wastewater, Environ. Sci. Technol. 55 (2021) 13231–13243.

[17] J. Li, G. Zhan, J. Yang, F. Quan, C. Mao, Y. Liu, B. Wang, F. Lei, L. Li, A.W.M. Chan, L. Xu, Y. Shi, Y. Du, W. Hao, P.K. Wong, J. Wang, S.X. Dou, L. Zhang, J.C. Yu, Efficient ammonia electrosynthesis from nitrate on strained ruthenium nanoclusters, J. Am. Chem. Soc. 142 (2020) 7036–7046.

[18] J. Gao, B. Jiang, C. Ni, Y. Qi, Y. Zhang, N. Oturan, M.A. Oturan, Non-precious Co3O4/Ti cathode based electrocatalytic nitrate reduction: preparation, performance and mechanism, Appl. Catal. B: Environ. 254 (2019) 391–402.

[19] J. Wang, C. Cai, Y. Wang, X. Yang, D. Wu, Y. Zhu, M. Li, M. Gu, M. Shao, Electrocatalytic reduction of nitrate to ammonia on low-cost ultrathin CoOx nanosheets, ACS Catal. 11 (2021) 15135–15140.

[20] R. Zhang, Y. Guo, S. Zhang, D. Chen, Y. Zhao, Z. Huang, L. Ma, P. Li, Q. Yang, G. Liang, C. Zhi, Efficient ammonia electrosynthesis and energy conversion through a Zn-nitrate battery by iron doping engineered nickel phosphide catalyst, Adv. Energ. Mater. 12 (2022), 2103872.

[21] Q. Yao, J. Chen, S. Xiao, Y. Zhang, X. Zhou, Selective electrocatalytic reduction of nitrate to ammonia with nickel phosphide, ACS Appl. Mater. Inter. 13 (2021) 30458–30467.

[22] Q. Liu, L. Xie, J. Liang, Y. Ren, Y. Wang, L. Zhang, L. Yue, T. Li, Y. Luo, N. Li, B. Tang, Y. Liu, S. Gao, A.A. Alshehri, I. Shakir, P.O. Agboola, Q. Kong, Q. Wang, D. Ma, X. Sun, Ambient ammonia synthesis via electrochemical reduction of nitrate enabled by NiCo2O4 nanowire array, Small 18 (2022), e2106961.

[23] S. Li, P. Ma, C. Gao, L. Liu, X. Wang, M. Shakouri, R. Chernikov, K. Wang, D. Liu, R. Ma, J. Wang, Reconstruction-induced NiCu-based catalysts towards paired electrochemical refining, Energ. Environ. Sci. 15 (2022) 3004–3014.

[24] S. Garcia-Segura, M. Lanzarini-Lopes, K. Hristovski, P. Westerhoff, Electrocatalytic reduction of nitrate: fundamentals to full-scale water treatment applications, Appl. Catal. B: Environ. 236 (2018) 546–568.

[25] Z.Y. Wu, M. Karamad, X. Yong, Q. Huang, D.A. Cullen, P. Zhu, C. Xia, Q. Xiao, M. Shakouri, F.-Y. Chen, J.Y.T. Kim, Y. Xia, K. Heck, Y. Hu, M.S. Wong, Q. Li, I. Gates, S. Siahrostami, H. Wang, Electrochemical ammonia synthesis via nitrate reduction on Fe single atom catalyst, Nat. Commun. 12 (2021) 2870.

[26] X. Zhang, Y. Wang, C. Liu, Y. Yu, S. Lu, B. Zhang, Recent advances in non-noble metal electrocatalysts for nitrate reduction, Chem. Eng. J. 403 (2021) 126269.

[27] X. Kong, H.Q. Peng, S. Bu, Q. Gao, T. Jiao, J. Cheng, B. Liu, G. Hong, C.S. Lee, W. Zhang, Defect engineering of nanostructured electrocatalysts for enhancing nitrogen reduction, J. Mater. Chem. A 8 (2020) 7457–7473.

[28] Y. Guo, R. Zhang, S. Zhang, Y. Zhao, Q. Yang, Z. Huang, B. Dong, C. Zhi, Pd doping-weakened intermediate adsorption to promote electrocatalytic nitrate reduction on TiO2 nanoarrays for ammonia production and energy supply with zinc–nitrate batteries, Energy Environ. Sci. 14 (2021) 3938–3944.

[29] T. Hu, M. Wang, C. Guo, C.M. Li, Functionalized MXenes for efficient electrocatalytic nitrate reduction to ammonia, J. Mater. Chem. A 10 (2022), 89238931.

[30] S. Yin, X. Zhao, E. Jiang, Y. Yan, P. Zhou, P. Huo, Boosting water decomposition by sulfur vacancies for efficient CO2 photoreduction, Energ, Environ. Sci. 15 (2022) 1556–1562.

[31] L. Li, Z. Qin, L. Ries, S. Hong, T. Michel, J. Yang, C. Salameh, M. Bechelany, P. Miele, D. Kaplan, M. Chhowalla, D. Voiry, Role of sulfur vacancies and undercoordinated Mo regions in MoS2 nanosheets toward the evolution of hydrogen, ACS Nano 13 (2019) 6824–6834.

[32] R. Jia, Y. Wang, C. Wang, Y. Ling, Y. Yu, B. Zhang, Boosting selective nitrate electroreduction to ammonium by constructing oxygen vacancies in TiO2, ACS Catal. 10 (2020) 3533–3540.

[33] Y. Wang, H. Li, W. Zhou, X. Zhang, B. Zhang, Y. Yu, Structurally disordered RuO2 nanosheets with rich oxygen vacancies for enhanced nitrate electroreduction to ammonia, Angew. Chem. Int. Ed. 61 (2022), e202202604.

[34] L. Zhou, M. Shao, C. Zhang, J. Zhao, S. He, D. Rao, M. Wei, D.G. Evans, X. Duan, Hierarchical CoNi-sulfide nanosheet arrays derived from layered double hydroxides toward efficient hydrazine electrooxidation, Adv. Mater. 29 (2017), 1604080.

[35] G. Zhou, Y. Hu, L. Long, P. Wang, Y. Shan, L. Wang, J. Guo, C. Zhang, Y. Zhang, L. Liu, Charged excited state induced by ultrathin nanotip drives highly efficient hydrogen evolution, Appl. Catal. B Environ. 262 (2020), 118305.

[36] H. Tao, C. Choi, L.X. Ding, Z. Jiang, Z. Han, M. Jia, Q. Fan, Y. Gao, H. Wang, A. W. Robertson, S. Hong, Y. Jung, S. Liu, Z. Sun, Nitrogen fixation by Ru singleatom electrocatalytic reduction, Chem 5 (2019) 204–214.

[37] C. Peng, G. Luo, J. Zhang, M. Chen, Z. Wang, T.K. Sham, L. Zhang, Y. Li, G. Zheng, Double sulfur vacancies by lithium tuning enhance CO2 electroreduction to n-propanol, Nat. Commun. 12 (2021) 1580.

[38] H.J. Li, Y.H. Song, K. Xi, W. Wang, S. Liu, G.R. Li, X.P. Gao, Sulfur vacancies in Co9S8−x/N-doped graphene enhancing the electrochemical kinetics for highperformance lithium–sulfur batteries, J. Mater. Chem. A 9 (2021) 10704–10713.

[39] F. Lu, M. Zhou, W. Li, Q. Weng, C. Li, Y. Xue, X. Jiang, X. Zeng, Y. Bando, D. Golberg, Engineering sulfur vacancies and impurities in NiCo2O4 nanostructures toward optimal supercapacitive performance, Nano Energy 26 (2016) 313–323.

[40] X. Feng, Q. Jiao, W. Chen, Y. Dang, Z. Dai, S.L. Suib, J. Zhang, Y. Zhao, H. Li, C. Feng, Cactus-like NiCo2S4@NiFe LDH hollow spheres as an effective oxygen bifunctional electrocatalyst in alkaline solution, Appl. Catal. B Environ. 286 (2021).

[41] M. You, S. Yi, X. Hou, Z. Wang, H. Ji, L. Zhang, Y. Wang, Z. Zhang, D. Chen, High temperature induced S vacancies in natural molybdenite for robust electrocatalytic nitrogen reduction, J. Colloid Interface Sci. 599 (2021) 849–856.

[42] W. Song, L. Fu, C. He, K. Xie, Carbon-coordinated single Cr site for efficient electrocatalytic N2 fixation, Adv. Theor. Simul. 4 (2021), 2100044.

[43] W. Zheng, Y. Liu, F. Liu, Y. Wang, N. Ren, S. You, Atomic hydrogen in electrocatalytic systems: generation, identification, and environmental applications, Water Res. 223 (2022), 118994.

[44] T. Zhu, Q. Chen, P. Liao, W. Duan, S. Liang, Z. Yan, C. Feng, Single-atom Cu catalysts for enhanced electrocatalytic nitrate reduction with significant alleviation of nitrite production, Small 16 (2020), e2004526.

[45] L. Fang, S. Wang, C. Song, X. Yang, Y. Li, H. Liu, Enhanced nitrate reduction reaction via efficient intermediate nitrite conversion on tunable CuxNiy/NC electrocatalysts, J. Hazard. Mater. 421 (2022), 126628.

[46] Y. Jiang, X. Wu, Y. Yan, S. Luo, X. Li, J. Huang, H. Zhang, D. Yang, Coupling PtNi ultrathin nanowires with MXenes for boosting electrocatalytic hydrogen evolution in both acidic and alkaline solutions, Small 15 (2019), 1805474.

[47] S. Zhang, M. Li, J. Li, Q. Song, X. Liu, High-ammonia selective metal-organic framework-derived Co-doped Fe/Fe2O3 catalysts for electrochemical nitrate reduction, P. Natl. Acad. Sci. USA 119 (2022), e2115504119.

[48] B. Xu, Z. Chen, G. Zhang, Y. Wang, On-demand atomic hydrogen provision by exposing electron-rich cobalt sites in an open-framework structure toward superior electrocatalytic nitrate conversion to dinitrogen, Environ. Sci. Technol. 56 (2022) 614–623.

[49] H. Liu, X. Lang, C. Zhu, J. Timoshenko, M. Ruscher, L. Bai, N. Guijarro, H. Yin, Y. Peng, J. Li, Z. Liu, W. Wang, B.R. Cuenya, J. Luo, Efficient electrochemical nitrate reduction to ammonia with copper-supported rhodium cluster and single-atom catalysts, Angew. Chem. Int. Ed. 61 (2022), e202202556.

[50] X. Zhang, C. Wang, Y. Guo, B. Zhang, Y. Wang, Y. Yu, Cu clusters/TiO2-x with abundant oxygen vacancies for enhanced electrocatalytic nitrate reduction to ammonia, J. Mater. Chem. A 10 (2022) 6448–6453.